



Deconvolution of Wave-Number-Frequency Spectra of Wall Pressure Fluctuations

Simon L. Prigent,* Édouard Salze,† and Christophe Bailly‡
Univ Lyon, Ecole Centrale de Lyon, LMFA UMR 5509, F-69134 Ecully, France

DOI: 10.2514/1.J058203

The wave-number-frequency spectra of a pressure field beneath a turbulent boundary layer is considered, with the aim of removing the effect of the measuring device. A rotating antenna of aligned microphones has been used in previous studies, and the measured spectra are shown to be a convolution of the true spectra with the transfer function of said antenna. Deconvolution algorithms that were previously developed for other fields of studies are presented. Test cases and processing of experimental data are used to assess their applicability. A hybrid approach of both deconvolution and interpolation, to artificially refine the azimuthal discretization, is found to be best at estimating both narrowband and broadband components of the spectra.

Nomenclature

\mathcal{F}	=	Fourier transform operator
h, \mathbf{H}	=	transfer function of antenna's geometry and its discrete form
k_0, k_c, c_0, U_c	=	acoustic and convective wave numbers, speed of sound, and convective velocity
p	=	wall pressure fluctuations
\hat{p}	=	frequency Fourier transform of wall pressure fluctuations
\tilde{p}	=	wave-number-frequency Fourier transform of wall pressure fluctuations
\mathcal{Q}	=	auxiliary function used during derivation of convolution product
R_{pp}	=	correlation function of wall pressure fluctuations
\mathcal{S}_f	=	reconstructed Fourier space
\mathcal{S}_m	=	measurement space, in which p and S_{pp} are sampled
S_{pp}	=	cross-spectral density of wall pressure fluctuations
\mathcal{S}_s	=	unbiased Fourier space
α, β	=	parameters of Corcos model
Φ_{pp}	=	wave-number-frequency spectra of wall pressure fluctuations
*	=	complex conjugate
<i>Subscripts</i>		
s, f, m	=	elements of $\mathcal{S}_s, \mathcal{S}_f,$ and \mathcal{S}_m
1, 2	=	first (streamwise) and second (transverse) directions of plane

I. Introduction

THE interest in wall pressure fluctuations goes back several decades [1,2], as it is key to understanding structural vibrations and vibroacoustic issues in applications ranging from hydrodynamics

to aeronautics as well as the rail and automotive industries. These fluctuations can be divided into the acoustic and hydrodynamic components, the former being induced by the acoustic waves impacting onto the wall and the latter directly by the turbulent boundary layer. The simultaneous study of both components is an experimental challenge, due to the large range of scales involved. In fact, most studies have focused on the hydrodynamic components and tried to offer a model for their spectra, such as that by Corcos [3]. However, the acoustic components, while of much lower amplitude, can play an important role for internal noise as it is commonly associated with radiating modes. Recent studies by Arguillat et al. [4] and Salze et al. [5,6] have offered a means to separate the two components from experimental measurements of a wall pressure field beneath a turbulent boundary layer. The authors have developed rotating antennas of microphones that allow the computation of the wave-number-frequency spectra of the fluctuations and offer a means to study both components separately for sufficiently high frequencies and/or Reynolds numbers.

As detailed by Salze et al. [5,6], such an antenna consists of a nonequidistant array of microphones that simultaneously record data to compute cross-spectra. Rotating the antenna with regard to the flow direction increases the number of different separation vectors that can be obtained through a combination of all microphone positions. Assuming homogeneity of the wall pressure field, the authors were able to use the large amount of separation vectors to perform a spatial Fourier transform of the cross-spectra, which gives the wave-number-frequency spectra. The latter thus depend on the number of separation vectors and their values, which is to say they depend on the geometry of the antenna.

In the field of beam forming, the use of deconvolution to recover the acoustic source maps from data biased by the geometry of a microphone array has been the topic of many studies [7–9], with DAMAS2 being a commonly used algorithm, introduced by Dougherty [10]. In particular, Ehrenfried and Koop [7] provided a detailed study on the application of such methods.

The use of wave-number-frequency spectra, however, is less common. Gabriel et al. [11] offered insight into the relative levels of the acoustic and hydrodynamic components thanks to measurements of such spectra. A recent numerical study by Cohen and Gloerfelt [12] has been focused on the influence of pressure gradients and offered new elements to the ongoing discussion of their impact on convection velocity. However, because of the inherent spatial resolution of such numerical simulations, the topic of deconvolution was not discussed. Another use of this approach was presented by Bahr and Cattafesta [13], who used this formalism to introduce a method of deconvolution of arbitrarily coherent acoustic sources by means of a wave-number-frequency covariance as an intermediate step in their algorithm. Some studies by Haxter and Spehr [14], and Ehrenfried and Koop [15] have looked directly into wave-number-frequency spectra from experimental measurements and have applied deconvolution to try and recover unbiased data. However, to the

Presented as Paper 2018-2899329 at the 2018 AIAA/CEAS Aeroacoustic Conferences, Atlanta, GA, 25–29 June 2018; received 13 December 2018; revision received 17 July 2019; accepted for publication 18 July 2019; published online 25 September 2019. Copyright © 2019 by Simon L. Prigent, Édouard Salze, and Christophe Bailly. Published by the American Institute of Aeronautics and Astronautics, Inc., with permission. All requests for copying and permission to reprint should be submitted to CCC at www.copyright.com; employ the eISSN 1533-385X to initiate your request. See also AIAA Rights and Permissions www.aiaa.org/randp.

*Postdoctoral Fellow.

†Research Engineer.

‡Professor. Senior Member AIAA.

authors' knowledge, there is still a number of uncertainties as to how to apply such deconvolution to wave-number-frequency spectra, and more details on parameters used in the algorithm itself are much needed.

The aim of this Paper is to investigate the applicability of common deconvolution algorithms, particularly DAMAS2, to the case of the wave-number-frequency spectra of wall pressure fluctuations beneath a turbulent boundary layer, measured by a rotating antenna such as that of Salze et al. [5,6]. Particular focus will be put on practical issues that can arise.

II. Convolution

A. Wave-Number-Frequency Transform

Physically speaking, there exists a pressure field $p(x,t)$, which has a wave-number-frequency transform \tilde{p}_s that can be defined in a $\mathbf{k}_s - \omega$ space referred to as the source space \mathcal{S}_s . The antenna of microphones samples this data from specific physical-space positions, to be processed as time-Fourier transforms \hat{p} . This measurement space \mathcal{S}_m is thus set in terms of $\mathbf{x} - \omega$. Once this space-frequency data is sampled, the reconstructed wave-number-frequency transform \tilde{p} can be computed and shall be expressed in terms of $\mathbf{k}_f - \omega$ in \mathcal{S}_f . The goal is thus to understand how the reconstructed transform \tilde{p}_f is linked to the preexisting unbiased transform \tilde{p}_s .

Analytically, and without the sampling constraints, the links between the mentioned transforms are expressed in terms of Fourier pairs as follows:

$$\begin{aligned}\tilde{p}_f(\mathbf{k}_f, \omega) &= \frac{1}{(2\pi)^2} \int_{\mathcal{S}_m} \hat{p}(\mathbf{x}, \omega) e^{-i\mathbf{k}_f \cdot \mathbf{x}} d\mathbf{x}, \\ \hat{p}(\mathbf{x}, \omega) &= \int_{\mathcal{S}_s} \tilde{p}_s(\mathbf{k}_s, \omega) e^{i\mathbf{k}_s \cdot \mathbf{x}} d\mathbf{k}_s\end{aligned}\quad (1)$$

Hence,

$$\begin{aligned}\tilde{p}_f(\mathbf{k}_f, \omega) &= \frac{1}{(2\pi)^2} \int_{\mathcal{S}_m} \int_{\mathcal{S}_s} \tilde{p}_s(\mathbf{k}_s, \omega) e^{i\mathbf{k}_s \cdot \mathbf{x}} d\mathbf{k}_s e^{-i\mathbf{k}_f \cdot \mathbf{x}} d\mathbf{x} \\ &= \int_{\mathcal{S}_s} \left(\int_{\mathcal{S}_m} \frac{1}{(2\pi)^2} e^{-i(\mathbf{k}_f - \mathbf{k}_s) \cdot \mathbf{x}} d\mathbf{x} \right) \tilde{p}_s(\mathbf{k}_s, \omega) d\mathbf{k}_s\end{aligned}$$

The link between the source and reconstructed wave-number-frequency transforms can thus be formulated as a convolution product on \mathbf{k} ,

$$\tilde{p}_f(\mathbf{k}, \omega) = (\tilde{p}_s \star h)(\mathbf{k}, \omega) \quad \text{where } h(\mathbf{k}) \equiv \frac{1}{(2\pi)^2} \int_{\mathcal{S}_m} e^{-i\mathbf{k} \cdot \mathbf{r}} d\mathbf{r} \quad (2)$$

is the antenna's transfer function. In the analytical case, and assuming the measurement space goes to infinity for both components of \mathbf{r} , the function h is equal to a Dirac distribution, $h(\mathbf{k}_f - \mathbf{k}_s) = \delta(\mathbf{k}_f - \mathbf{k}_s)$. As a result, one obtains the relation $\tilde{p}_f = \tilde{p}_s$. In practice, the measurements are performed with a finite number of points, set by the antenna's geometry, that will require a discretization of Eq. (2). In this regard, the convolution function h is not a Dirac distribution anymore and becomes the transfer function of the antenna's geometry.

B. Wave-Number-Frequency Spectra

The wave-number-frequency spectrum Φ_{pp} is defined as the space-time Fourier transform of the correlation function R_{pp} :

$$\Phi_{pp}(\mathbf{k}, \omega) \equiv \frac{1}{(2\pi)^3} \int_{\mathcal{S}_m} \int_{-\infty}^{+\infty} R_{pp}(\mathbf{r}, \tau) e^{-i(\mathbf{k} \cdot \mathbf{r} - \omega \tau)} d\tau d\mathbf{r} \quad (3)$$

Two approaches can be taken to compute this spectrum. First, one can start by performing the time-Fourier transform of the correlation

function to obtain the cross-spectral density, $S_{pp}(\mathbf{r}, \omega)$. In practice, it can be estimated by

$$S_{pp}(\mathbf{x}, \mathbf{r}, \omega) \equiv 2\pi E [\hat{p}(\mathbf{x}, \omega) \hat{p}^*(\mathbf{x} + \mathbf{r}, \omega)] \quad (4)$$

for broadband signals and assuming $S_{pp}(\mathbf{x}, \mathbf{r}, \omega) = S_{pp}(\mathbf{r}, \omega)$ for a homogeneous wall pressure field. E stands for the expected value operator and contains the limit for the time extent T going to infinity and the $1/T$ factor that one would use in a sample average formulation. The wave-number-frequency spectra are then simply computed by space-Fourier transforming the cross-spectra:

$$\Phi_{f,pp}(\mathbf{k}, \omega) = \frac{1}{(2\pi)^2} \int_{\mathcal{S}_m} S_{pp}(\mathbf{r}, \omega) e^{-i\mathbf{k} \cdot \mathbf{r}} d\mathbf{r}$$

A second approach [16] is to use a definition akin to that from Eq. (4) that would yield

$$\Phi_{f,pp}(\mathbf{k}, \omega) = (2\pi)^3 E[\tilde{p}(\mathbf{k}, \omega) \tilde{p}^*(\mathbf{k}, \omega)]$$

While both approaches are theoretically equivalent, their applicability differs from case to case, and they lead to distinct convolution relations. Indeed, the latter requires two space-Fourier transforms to be computed, and the former only one, which translates into different formulations of the transfer functions.

In the present Paper, the wall pressure field cannot be synchronously measured at different angular positions of the antenna, which prevents performing the space-Fourier transform first. In addition, computing the expected value over time in Eq. (4) requires long time signals, which are rather easy to record with microphones; however, its equivalent formulation in space would have required a larger measurement field than available. The first approach is thus selected, and the following establishes the convolution relation for the wave-number-frequency spectra within the frame of this study.

For ease of notation, one can consider the auxiliary function:

$$\mathcal{Q}_f(\mathbf{k}, \omega) = \int_{\mathcal{S}_m} \hat{p}(0, \omega) \hat{p}^*(\mathbf{r}, \omega) e^{-i\mathbf{k} \cdot \mathbf{r}} d\mathbf{r}$$

Using Eq. (1), $\mathcal{Q}_f(\mathbf{k}_f, \omega)$ can be calculated as

$$\begin{aligned}\mathcal{Q}_f(\mathbf{k}_f, \omega) &= \hat{p}(0, \omega) \int_{\mathcal{S}_m} \left(\int_{\mathcal{S}_s} \tilde{p}_s(\mathbf{k}_s, \omega) e^{i\mathbf{k}_s \cdot \mathbf{r}} d\mathbf{k}_s \right)^* e^{-i\mathbf{k}_f \cdot \mathbf{r}} d\mathbf{r} \\ &= \hat{p}(0, \omega) \int_{\mathcal{S}_m} \int_{\mathcal{S}_s} \tilde{p}_s^*(\mathbf{k}_s, \omega) e^{-i\mathbf{k}_s \cdot \mathbf{r}} d\mathbf{k}_s e^{-i\mathbf{k}_f \cdot \mathbf{r}} d\mathbf{r} \\ &= -\hat{p}(0, \omega) \int_{\mathcal{S}_m} \int_{\mathcal{S}_s} \tilde{p}_s^*(-\mathbf{k}_s, \omega) e^{-i(\mathbf{k}_f - \mathbf{k}_s) \cdot \mathbf{r}} d\mathbf{k}_s d\mathbf{r}\end{aligned}$$

by the change of variable $-\mathbf{k}_s$ to \mathbf{k}_s . One can now consider the associated function in the source space

$$\begin{aligned}\mathcal{Q}_s(\mathbf{k}_s, \omega) &= \int_{\mathcal{S}_m} \hat{p}(0, \omega) \hat{p}^*(\mathbf{r}, \omega) e^{-i\mathbf{k}_s \cdot \mathbf{r}} d\mathbf{r} \\ &= -\hat{p}(0, \omega) \left(\int_{\mathcal{S}_m} \hat{p}(-\mathbf{r}, \omega) e^{-i\mathbf{k}_s \cdot \mathbf{r}} d\mathbf{r} \right)^* \\ &= -(2\pi)^2 \hat{p}(0, \omega) \tilde{p}_s^*(-\mathbf{k}_s, \omega)\end{aligned}$$

One has

$$\begin{aligned}\int_{\mathcal{S}_s} \mathcal{Q}_s(\mathbf{k}_s, \omega) h(\mathbf{k}_f - \mathbf{k}_s) d\mathbf{k}_s \\ &= -\hat{p}(0, \omega) \int_{\mathcal{S}_s} \tilde{p}_s^*(-\mathbf{k}_s, \omega) \int_{\mathcal{S}_m} e^{-i(\mathbf{k}_f - \mathbf{k}_s) \cdot \mathbf{r}} d\mathbf{r} d\mathbf{k}_s \\ &= -\hat{p}(0, \omega) \int_{\mathcal{S}_m} \int_{\mathcal{S}_s} \tilde{p}_s^*(-\mathbf{k}_s, \omega) e^{-i(\mathbf{k}_f - \mathbf{k}_s) \cdot \mathbf{r}} d\mathbf{k}_s d\mathbf{r}\end{aligned}$$

Thus,

$$\mathcal{Q}_f(\mathbf{k}, \omega) = (\mathcal{Q}_s \star h)(\mathbf{k}, \omega)$$

The convolution problem for the wave-number-frequency spectra is set as

$$\Phi_{f,pp} = \Phi_{s,pp} \star h \quad (5)$$

with h defined in Eq. (2) and $\Phi_{s,pp}$ being the unbiased spectra. It is worth noting that the transfer function h is the same for both wave-number-frequency spectra and transforms. At this stage, h is known since \mathbf{r} and \mathbf{k} are given by the antenna's geometry and the processing scheme, respectively. $\Phi_{f,pp}$ is measured, and therefore only $\Phi_{s,pp}$ is an unknown of this convolution problem. Note that by using the symmetry of the antenna and the assumed homogeneity of the pressure field one finds, as expected, that both quantities h and $\Phi_{f,pp}$ are real.

III. Discrete Problem

The antenna of reference in the current study consists of 63 microphones aligned on a rotating disk, as detailed by Salze et al. [5,6]. For each angular position θ_m , a separation vector \mathbf{r}_{nm} is obtained from each possible combination of microphones and is used to calculate R_{pp} as illustrated in Fig. 1. The spectrum defined in Eq. (3) can thus be discretized on \mathbf{r}_{nm} ,

$$\Phi_{f,pp}(\mathbf{k}, \omega) = \frac{1}{(2\pi)^2} \sum_m \sum_n w_n S_{pp}(\mathbf{r}_{nm}, \omega) e^{-i\mathbf{k} \cdot \mathbf{r}_{nm}} ds_n \quad (6)$$

along with the transfer function

$$h(\mathbf{k}) = \frac{1}{(2\pi)^2} \sum_m \sum_n w_n e^{-i\mathbf{k} \cdot \mathbf{r}_{nm}} ds_n \quad (7)$$

where ds_n represents the local area around the point of summation and w_n represents a window function. The importance of windowing is discussed later. A Cartesian \mathbf{k} grid is then introduced, and the element $\mathbf{H}_{i,j}$ corresponds to $h(\{k_1(j), k_2(i)\})$ calculated with the previous equation. This discretization is the cause of the geometric bias introduced by the antenna and that needs correcting.

The obtained formulation is akin to that of a beam forming approach, which is commonly used for acoustic sources localization. In his study of deconvolution techniques for beam forming, Dougherty [10] presented two methods: one based on the application of a spectral filter and the other being a new version of the common iterative deconvolution process called DAMAS. Both methods are introduced and applied to the wave-number-frequency spectra in the following sections.

A. Algorithms for Deconvolution

In both deconvolution approaches presented hereafter, a dual Fourier space is introduced to reduce computation efforts thanks to

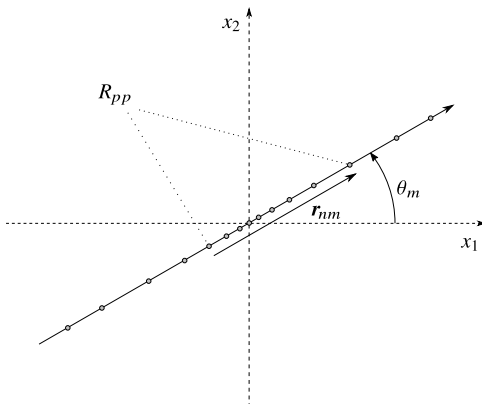


Fig. 1 Sketch of the rotating antenna.

the convolution theorem. For this space, the direct \mathcal{F} and inverse \mathcal{F}^{-1} Fourier operators are defined as follows:

$$\mathcal{F}(\Phi_{s,pp})(\boldsymbol{\xi}, \omega) = \int \Phi_{s,pp}(\mathbf{k}, \omega) e^{-i\mathbf{k} \cdot \boldsymbol{\xi}} d\mathbf{k} \quad (8)$$

$$\begin{aligned} \Phi_{s,pp}(\mathbf{k}, \omega) &= \mathcal{F}^{-1}[\mathcal{F}(\Phi_{s,pp})](\mathbf{k}, \omega) \\ &= \frac{1}{(2\pi)^2} \int \mathcal{F}(\Phi_{s,pp})(\boldsymbol{\xi}, \omega) e^{i\mathbf{k} \cdot \boldsymbol{\xi}} d\boldsymbol{\xi} \end{aligned}$$

1. Wiener Filter

Equation (5) can be directly inverted by using a Wiener filtering method in the dual Fourier space. A regularization term is commonly introduced in the denominator [17], which yields

$$\mathcal{F}(\Phi_{s,pp}) = \left[\frac{\mathcal{F}(h)^*}{|\mathcal{F}(h)|^2 + \gamma} \right] \mathcal{F}(\Phi_{f,pp})$$

where γ is a scalar constant linked to the signal-to-noise ratio.

2. DAMAS2

Equation (5) can also be inverted by using an iterative algorithm. The underlying mathematical idea is detailed by Schafer et al. [18] and can be roughly summarized as follows, leaving aside important considerations that the reader is encouraged to read. The convolution from Eq. (5) can be written as an operator D and the constraints on $\Phi_{s,pp}$, i.e., positivity of the spectra, expressed by means of an operator C :

$$\begin{cases} \Phi_{f,pp} = D\Phi_{s,pp} \\ \Phi_{s,pp} = C\Phi_{s,pp} \end{cases} \quad (9)$$

A linear combination of those relations yields

$$\Phi_{s,pp} = C\Phi_{s,pp} + \frac{1}{a}(\Phi_{f,pp} - DC\Phi_{s,pp}) \equiv L\Phi_{s,pp} \quad (10)$$

where a is a relaxation parameter used to control the convergence of an iterative series based on the latter equation. Indeed, if the operator L is a contraction, there exists a unique fixed point, and any sequence $\Phi_{s,pp}^{(n+1)} = L\Phi_{s,pp}^{(n)}$ shall converge toward it.

This is the basis for many deconvolution approaches developed for acoustic sources localization by microphones arrays [7–9,14]. The DAMAS algorithm by Brooks and Humphreys [19,20] is widely used in aeroacoustics, and its extension DAMAS2 [10] takes advantage of the convolution theorem to perform multiplication in a Fourier space instead of convolution product in the original space. In practice, the process is as follows [10], but the Gaussian filter introduced in the dual Fourier space is disregarded here.

The positive real constant a is computed as

$$a = \sum_{i,j} |\mathbf{H}_{i,j}| \quad (11)$$

The iterative algorithm is then obtained from $\Phi_{s,pp}^{(n)}$ to $\Phi_{s,pp}^{(n+1)}$ by calculating

$$\begin{cases} b = \mathcal{F}^{-1}[\mathcal{F}(\Phi_{s,pp}^{(n)})\mathcal{F}(h)] \\ \Phi_{s,pp}^{(n+1/2)} = \Phi_{s,pp}^{(n)} + \frac{1}{a}(\Phi_{f,pp} - b) \\ \Phi_{s,pp}^{(n+1)} = \max(\Phi_{s,pp}^{(n+1/2)}, 0) \end{cases} \quad (12)$$

B. Analytical Test Cases

For the purpose of testing the method and applicability of the mentioned algorithms to the wave-number-frequency spectra of wall pressure fluctuations beneath a turbulent boundary layer, analytical

test cases are taken as a combination of an acoustic diffuse field and a Corcos-like pressure field such that $S_{pp} = S_{\text{dif}} + S_{\text{cor}}$ with

$$S_{\text{dif}}(\mathbf{r}, \omega) = A \frac{\sin(k_0 |\mathbf{r}|)}{k_0 |\mathbf{r}|} \quad S_{\text{cor}}(\mathbf{r}, \omega) = e^{-k_c |\mathbf{r}_1| / \alpha} e^{-k_c |\mathbf{r}_2| / \beta} e^{ik_c r_1}$$

where the constant A is linked to the energy ratio between the two fields. The change of sign of the model's imaginary part from its original expression proposed by Corcos [3] is due to the current Fourier transform convention. The analytical expressions of the corresponding spectra are

$$\Phi_{\text{dif}} = \begin{cases} \frac{A}{2\pi k_0^2} \frac{1}{\sqrt{1-(|k|/k_0)^2}} & \text{if } |k| < k_0 \\ 0 & \text{if } |k| > k_0 \end{cases}$$

$$\Phi_{\text{cor}} = \frac{1}{\pi^2} \frac{\alpha k_c}{k_c^2 + \alpha^2 (k_1 - k_c)^2} \frac{\beta k_c}{k_c^2 + \beta^2 k_2^2}$$

The array geometry that will be taken for this study is that of the rotating antenna from Salze et al. [5,6]. To match with these previous experimental campaigns, and unless stated otherwise in specific sections of this Paper, the following parameters were used: $f = 3750$ Hz, $U_c = 0.7 \cdot 75$ m \cdot s $^{-1}$, $c_0 = 342.6$ m \cdot s $^{-1}$, $\alpha = 8$, $\beta = 1$, and $A = 0.01$. Note that for a convenient use of the FFT and iFFT algorithms, the tests have been carried on square data matrices. For ease of visualization, some datasets are then only displayed for $-200 < k_1 < 800$ m $^{-1}$.

C. Windowing and Angular Resolution

Two important aspects of the discretization have voluntarily been left unaddressed so far: the angular resolution of the antenna and the window function used in Eq. (7). They play a role in the sampling and processing of the data and directly affect h and therefore $\Phi_{f,pp}$. While performing the space-Fourier transform, the extent over which data has been sampled is inherently limited, and not using a window function in the discrete sum would de facto correspond to applying a rectangular window to the data. The minimum four-term Blackman–Harris window is chosen for the rest of the Paper; it is commonly used in many applications and has a relative sidelobe attenuation of -92 dB [21]. The regularization of the window depends on the method used to process data; in this Paper's case, the wave-number-frequency spectrum is obtained from the cross-spectral density with a Blackman–Tukey method, which is a type of correlogram-based method. In this case, no regularization is required so long as $w(\mathbf{r} = 0) = 1$. Naturally, in the present Paper, the data is not only sampled over a limited physical extent but also nonuniformly sampled, which will add to the outcome bias.

The transfer function h computed with and without windowing, at an azimuthal resolution of $\pi/64$, is depicted in Fig. 2a. When using the minimum four-term Blackman–Harris window, the transfer function shows a peak that monotonously falls to low values. On the other hand, with no window applied, strong oscillations that arise

from the Fourier transform of the rectangular window are observed. One also notices the offset for $|k| > 500$ m $^{-1}$, clearly visible in the case without windowing. That offset is linked to the azimuthal discretization and not the radial one as per the oscillations.

Indeed, the angular resolution, that is to say, the azimuthal discretization, is directly linked to radial spokes in the transfer function. These spokes only appear for a high amplitude of $|k|$ [22], after a threshold that depends on the angular steps. Therefore, the more refined the azimuthal discretization, the farther away these spokes are pushed. Figure 2b shows indeed that for coarse azimuthal resolutions h exhibits an offset from its low-value plateau. The threshold value of $|k|$ for this offset increases with refined resolutions and is no longer within the range of interest at $\pi/127$. It is worth noting that h does not exactly reach zero values and that the plateau is lowered with refined resolution, which will logically affect the outcome of the convolution product. A resolution of $\pi/127$ is thus the coarser that should be used in the present case.

The effects of the azimuthal discretization observed on h are directly impacting the estimated wave-number-frequency spectra, according to Eq. (5). Figure 3 shows profiles of the wave-number-frequency spectra estimated with various values of angular resolution and their analytically calculated counterpart. One should note the spectra are displayed before any form of deconvolution.

While the acoustic region does not seem to be affected by the change in resolution, the convective ridge clearly is strongly affected. The $\pi/32$ calculation overestimates the value of the spectra by about 36% in the convective part. The overestimate appears to be reduced by 3 from $\pi/32$ to $\pi/64$ and from $\pi/64$ to $\pi/127$; however, the $\pi/235$ resolution slightly underestimates the level of the convective ridge. It thus seems that $\pi/127$ offers a good compromise. Given that in the experimental campaigns motivating the present Paper [5,6] the angular resolution was $\pi/64$, the effect of sampling at this resolution and then linearly interpolating the data to $\pi/127$ is also displayed in Fig. 3. While the outcome slightly differs from the case of directly sampling at $\pi/127$, the change is rather small, and this approach should thus be taken for the processing of experimental data.

IV. Results

A. Results from Wiener Filter

Deconvolution with the Wiener filter can be applied to the test cases, as previously presented, with the parameter γ still to be adjusted to render the most accurate results possible. To this end, Fig. 4 shows $k_2 = 0$ and $k_1 = k_c$ profiles of the spectra for the synthetic data sampled as per the antenna geometry, before and after deconvolution with different values of γ and the analytical profiles for comparison.

The initial value $\gamma = 0.1$ clearly gives the worst results with a strong underestimation of both the acoustic peaks and the convective ridge. Lower values, from $\gamma = 0.01$ to 0.0001, show little effect on the convective ridge, with a better estimation of the acoustic peaks. The value 0.001 appears to be the best compromise, since it renders a value close to the analytical solution on the convective ridge and

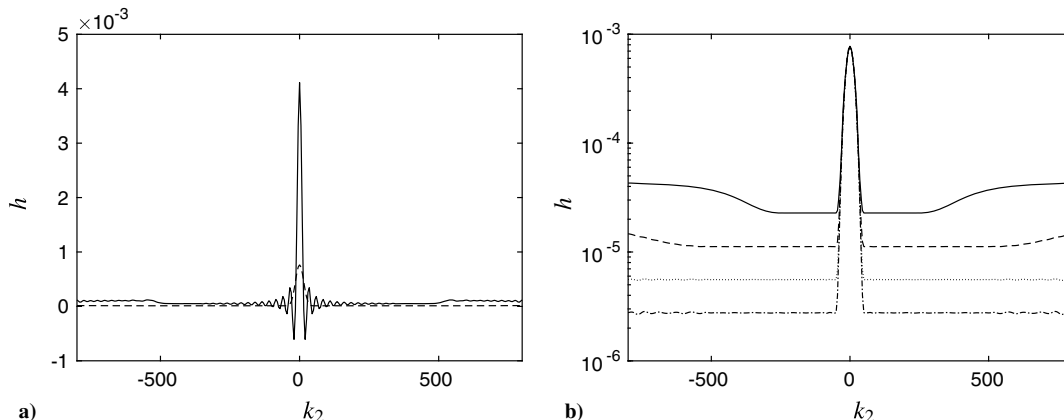


Fig. 2 Transfer function h computed a) with a $\pi/64$ angular resolution — without and ---- with windowing and b) with windowing at various angular resolution: — $\pi/32$, ---- $\pi/64$, $\pi/127$, and -.-.- $\pi/235$.

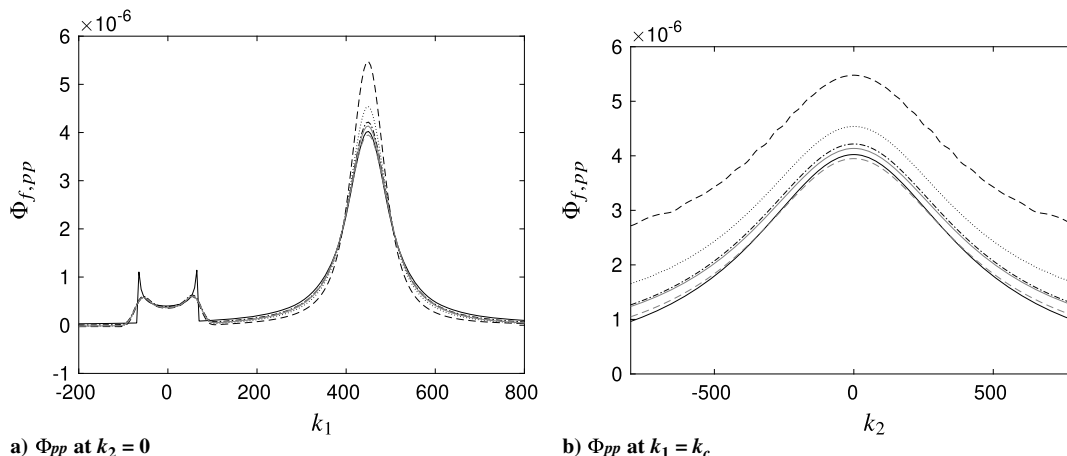


Fig. 3 Profiles of the spectra before deconvolution for different angular resolutions. — analytic, - - - $\pi/32$, ···· $\pi/64$, - · - $\pi/64$ interpolated to $\pi/127$, — — — $\pi/253$.

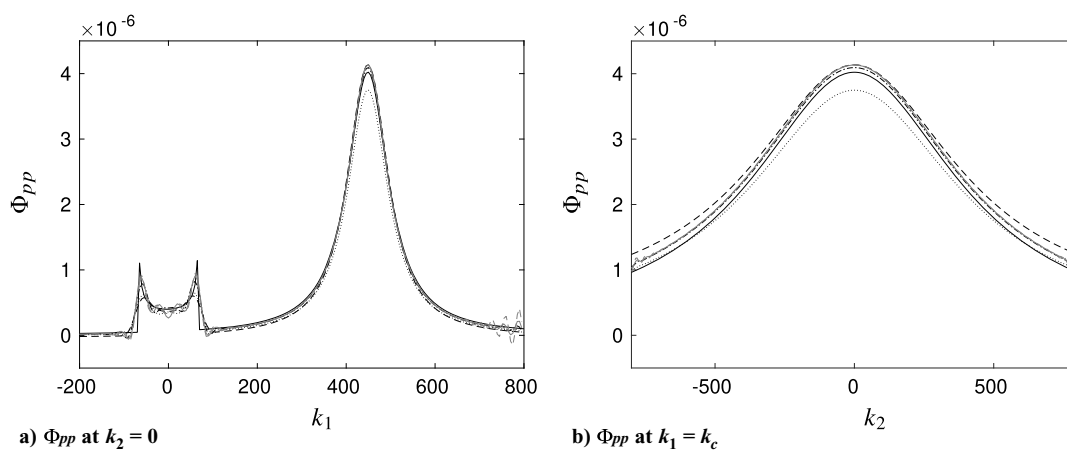


Fig. 4 Spectra deconvolved with Wiener filters: cross plots. — analytic, - - - array sampled, ···· $\gamma = 0.1$, - · - $\gamma = 0.01$, — — — $\gamma = 0.0001$.

limits high wave numbers' oscillations, while satisfactorily rendering the acoustic peaks.

Figure 5 shows the full spectra before and after deconvolution with the Wiener filter. As was seen on the profiles, the convective ridge is not affected, while the acoustic region is sharpened, at the cost of a mild radial oscillation.

B. Initials Results from DAMAS2

With DAMAS2 being an iterative process, it is important to define a criterion to stop the loop. To this end, the value $\sum_{i,j} (\Phi_{f,pp} - b)/a$ from the iterative steps shall be followed and henceforth referred to as residual. The following sections look into some key aspects of the algorithms and its applications, along with some potential limitations.

1. Relaxation Parameter

The relaxation parameter a sets the rate of convergence of the iterative algorithm previously mentioned and can be freely chosen with the constraint that the operator L must remain a contraction. For DAMAS2, Dougherty [10] has used the definition given in Eq. (11). Alternatively, Schafer et al. [18] suggest the use of $\max(\mathcal{F}(\mathbf{H})_{i,j})$. The present Paper, however, requires the use of a dual Fourier space that transforms the convolution in \mathbf{k} space into a product in $\boldsymbol{\zeta}$ space, while the original algorithms move from \mathbf{x} space to \mathbf{k} space. With the definition given in Eq. (8), there is a $(2\pi)^2$ factor between the two cases that is going to affect b in the iterative algorithm and in turn also affect a ; see Eq. (12). Dougherty's definition gives $a = 0.0648$, and multiplied by $(2\pi)^2$, $a = 2.5582$. Schafer et al.'s definition gives 43.25 once multiplied by $(2\pi)^2$.

The effect of a on the convergence of the deconvolution algorithm is illustrated in Fig. 6 with the two previously discussed definitions and

an arbitrarily high value. The residual has been defined previously, and the energy refers to the integral over both k_1 and k_2 of the modified spectra at each iteration. The former is normalized by its first value to allow comparison, and the latter is normalized by its equivalent taken from the analytical spectra. The lowest discussed value $a = 0.0648$ does not converge, and its erratic outcome is not depicted in Fig. 6 to avoid confusion. In all three presented cases, the residual indeed converges toward a plateau. While the lowest displayed value of a satisfactorily converges and is kept for the remainder of the Paper, a higher value could also be used without any expected change in the results and at a cost in terms of additional required iterations that is only a matter of seconds and is therefore not prohibitive.

Figure 7 shows profiles of the spectra deconvolved after a bespoke number of iterations, based on the convergence observed in Fig. 6. While the deconvolution does not affect the maximum value of the convective ridge, the subconvective region is clearly improved, which is of importance for matters of vibroacoustics [23]. The acoustic region is also better rendered, at the cost of small oscillations; the peaks are more accurately resolved, and their level is better estimated. The different values of a lead to quasi-identical outputs, at the exception of the small added oscillations which amplitude vary from case to case. When too many iterations are applied, the outcome is downgraded with strong spurious oscillations. In fact, although a plateau is reached for the residual and the energy, it appears that a very slight divergence starts at high values of iterations. One should therefore take the smallest possible number of iterations that is on the plateau.

2. Filtering

In the original algorithm of DAMAS2, a Gaussian filter is introduced in the dual Fourier space and has not been used in the

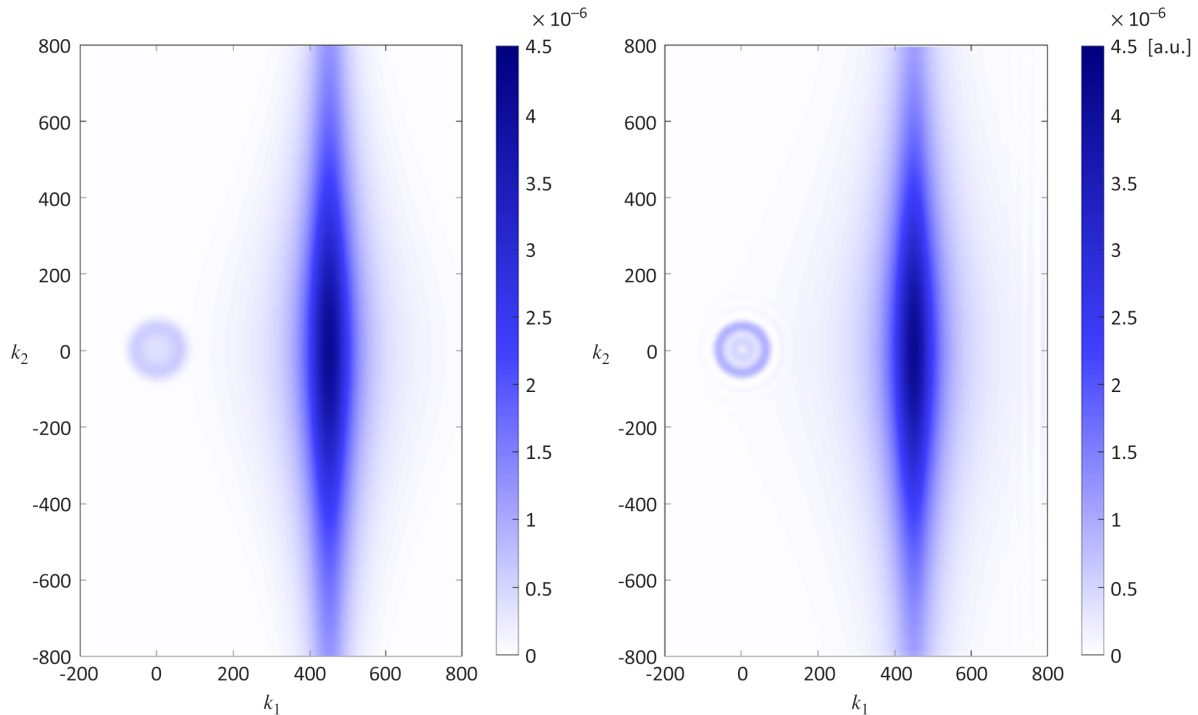


Fig. 5 Φ_{pp} $\pi/127$, before (left) and after (right) deconvolution with a Wiener filter $\gamma = 0.001$.

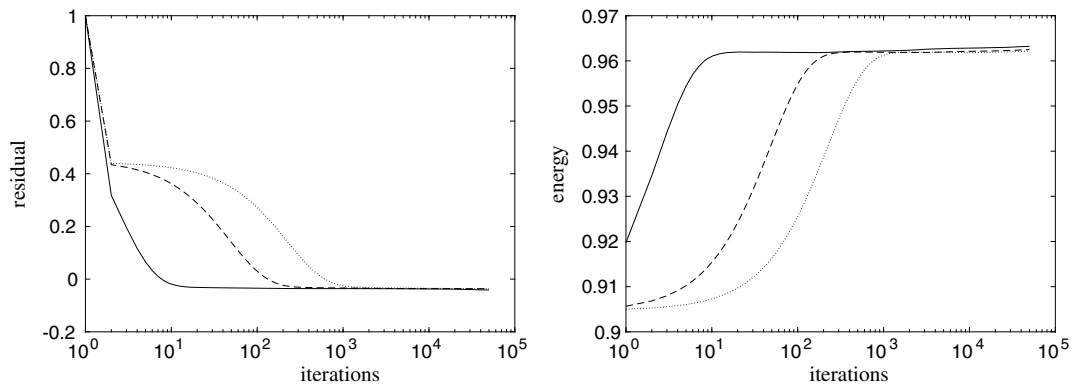


Fig. 6 Normalized residual (left) and energy (right) during deconvolution of the $\pi/127$ case for — $a = 2.558$, ---- $a = 43.25$, and $a = 200$.

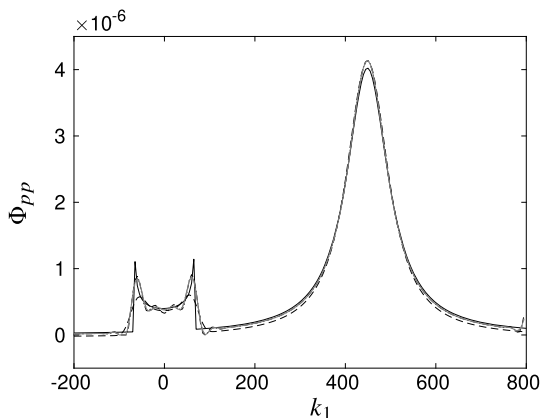


Fig. 7 Deconvolved Φ_{pp} profiles at $k_2 = 0$, with analytic and array-sampled ones for comparison. — analytic, ---- array-sampled, $a = 2.558$, — $a = 43.25$, and ---- $a = 200$.

present Paper. While it does not prevent the convergence, and only changes the number of required iterations for a given value of a , it has not proven useful within the frame of this Paper. Indeed, the output of the deconvolution is not qualitatively affected, and the same small oscillations that have been previously discussed remain. The level of

the output, on the other hand, is strongly affected by the width selected for the Gaussian filter. In this regard, one should be careful to use the proper normalization when including this filter in the deconvolution algorithm.

C. Effect of Frequency: Deconvolution vs Bettered Azimuthal Resolution

All previous test cases were conducted at a frequency of 3750 Hz. Figure 8 shows the $k_2 = 0$ profiles of Φ_{pp} after deconvolution for different frequencies. Although convergence of the deconvolution is indeed reached in all cases, the number of needed iterations is dramatically increased at low frequencies, with up to 10,000 iterations required for the 500 Hz case.

At this low frequency, one notices that the array-sampled profile barely displays anything in the acoustic region and is underestimating the peak value of the convective ridge by more than a factor of 2. It is thus clear that the angular refinement previously discussed has reached its limits and the deconvolution is more efficient at recovering the narrowband peaks of both the acoustic and convective regions. When increasing the frequency, the underestimation of the convective ridge is reduced, and the acoustic region is detected, despite its level being wrongly estimated; the deconvolution is still useful for both the acoustic and convective regions. At 4 kHz, on the other hand, the array-sampled convective ridge is not affected by the

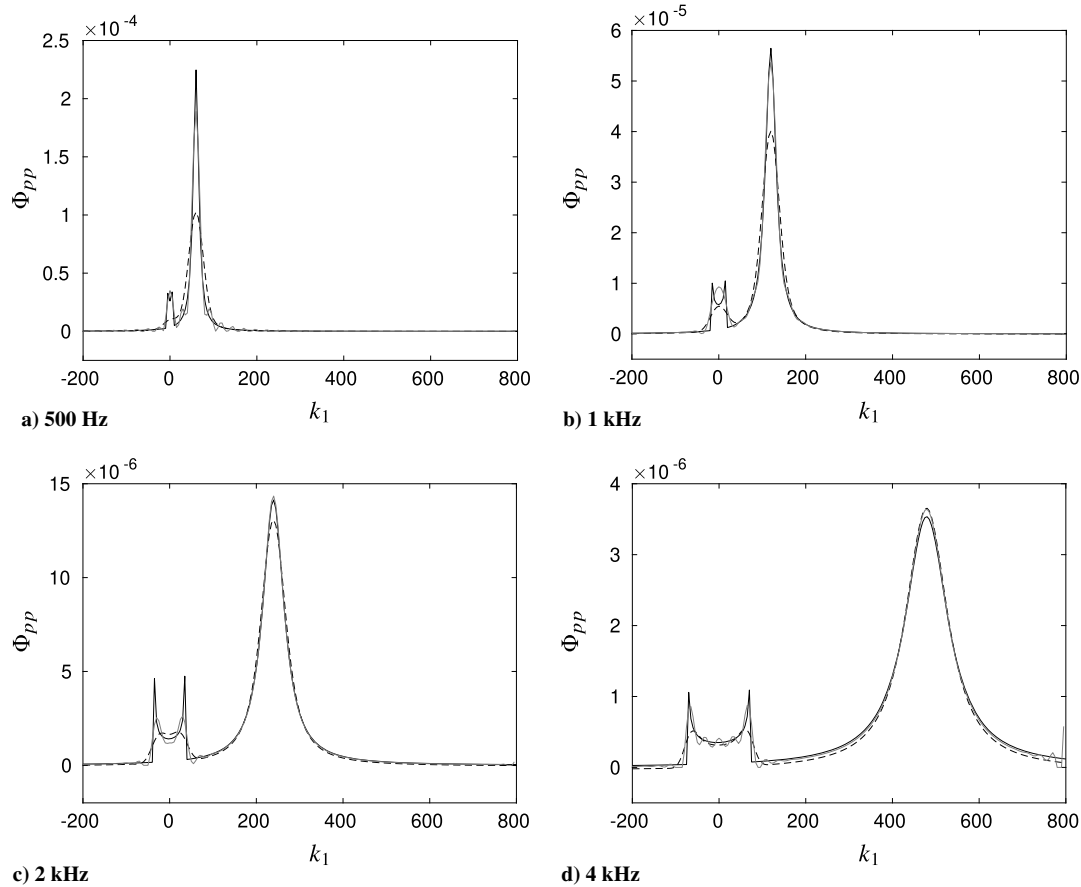


Fig. 8 Profiles of Φ_{pp} deconvolved with DAMAS2 at various frequencies. — analytic, - - - array-sampled, and - · - deconvolved.

deconvolution, its peak values being also well estimated thanks to the refined azimuthal discretization. The subconvective region is improved with deconvolution, however, and the narrow peaks of the acoustic regions are more precisely estimated.

Since the deconvolution appears useful in most cases, and not detrimental to the broadband ridge, one could wonder why it is not directly applied without the refinement of azimuthal discretization. Figure 9 shows profiles of the spectra estimated at $\pi/64$ then deconvolved alongside the results of deconvolution for $\pi/127$ and the analytical spectra for reference. The initial overestimation of the convective ridge is partially corrected by the deconvolution; however, the outcome is still higher than that obtained by deconvolution of the $\pi/127$ estimation. The subconvective and acoustic regions, on the other hand, exhibit little difference between the two cases.

As side note, it should be said that the convergence of deconvolution for the $\pi/64$ case is not as straightforward as that

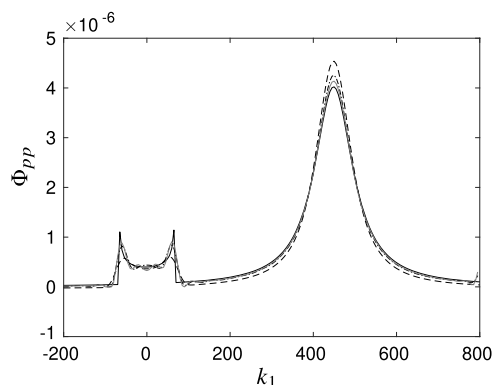


Fig. 9 Profiles of Φ_{pp} at two azimuthal resolutions, with deconvolution. — analytic, - - - array sampled $\pi/64$, - · - $\pi/64$ deconvolved, and - · - $\pi/127$ deconvolved.

previously discussed. Indeed, while both residual and energy initially tend toward a plateau, this stable state is only maintained for a short extent of iterations and quickly diverges afterward. One should thus be careful in that case to choose a suited number of iterations.

These observations show that for broadband components, such as the convective ridge at high frequencies, the refinement of azimuthal discretization is key, while the deconvolution will serve to correct the estimation of narrowband peaks, more relevant for the acoustic region or at relatively low frequencies. Naturally, the notion of low or high frequency here is relative to the k grid on which the spectra are projected, and defining a threshold would be a rather slippery approach. A hybrid method of both azimuthal refinement and deconvolution is thus recommended.

D. Acoustic Level

Another parameter that is not directly linked to the deconvolution but rather to the ability of the antenna to resolve the spectra correctly is the relative acoustic level, previously noted A . Figure 10 shows the acoustic region for four values of this relative level. The previous tests were conducted with $A = 0.01$, and it is indeed shown to be correctly resolved. However, when reaching $A = 0.001$, it is clear that the acoustic contribution is more strongly affected by the tail of the hydrodynamic one and that overall its resolution is of lesser quality. The more extreme case of $A = 0.0001$ leads to the same conclusion with a barely resolved acoustic contribution. It is thus safe to say that below a threshold of $A = 0.001$ an attempt to look at the acoustic region should be conducted with caution.

V. Application to Experimental Data

Datasets from previous experimental campaigns are used to test the applicability of the discussed methods. Wall pressure measurements were conducted, within the SONOBL project, in a test section designed to create a zero-pressure gradient boundary layer, placed in the anechoic chamber of the Centre Acoustique of Ecole Centrale de

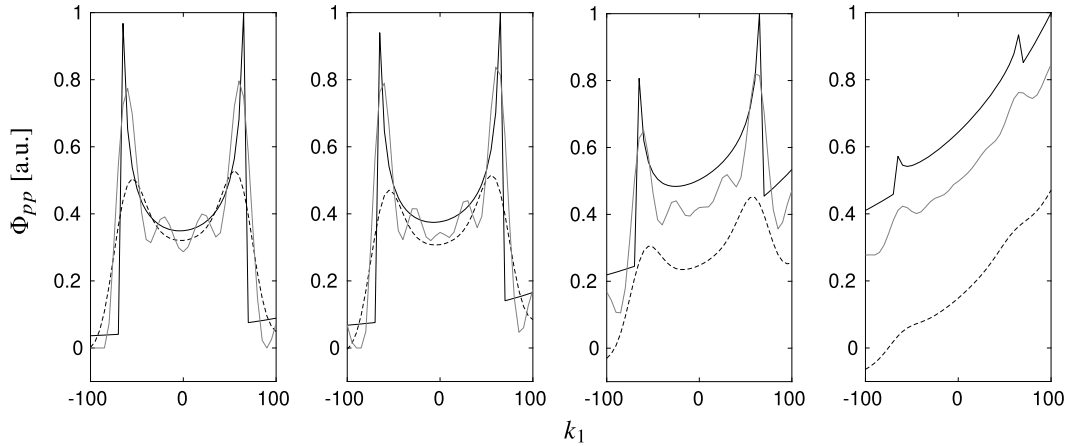


Fig. 10 Spectra ($k_2 = 0$) with various acoustic levels, zoomed in on the acoustic region and normalized by the local maximum. From left to right: $A = 0.01$, $A = 0.005$, $A = 0.001$, and $A = 0.0001$. — analytic, ---- array sampled, and deconvolved.

Lyon. A rotating antenna of 63 microphones placed in line sampled the data with a $\pi/64$ angular resolution. Further details on the setup can be found in the studies by Salze et al. [5,6]. The following is taken at 3750 Hz for the zero-pressure gradient case at $75 \text{ m} \cdot \text{s}^{-1}$.

Following from the analytical test cases, the experimental data is linearly interpolated to an azimuthal resolution of $\pi/127$ and then deconvolved with DAMAS2. The evolution of the residual during the deconvolution is provided in Fig. 11a, which indicates that 3400 iterations are required. Similarly to the analytical cases, taking a larger value for a would have also converged, simply requiring more iterations. Figure 11b shows profiles of the spectra before and after deconvolution. As noted before, the deconvolution has little effect on the convective ridge, while the acoustic region is strongly affected where the measured peaks are sharpened. It is worth noticing, though, that some peaks appear in the subconvective region; they are most likely spurious ones due to an amplification of background oscillations.

Both spectra are fully displayed in Fig. 12. While the deconvolution makes the overall aspect noisier, its sharpening the data makes the acoustic region more resolved. It is indeed possible to see clear components, not only at $k = 0$ but also on or within the acoustic circle.

Overall, the DAMAS2 algorithm appears to behave similarly with the experimental data as it does with the analytical test cases previously conducted.

A similar test is then conducted with the Wiener filter, setting $\gamma = 0.001$ based on the analytical test cases. Figure 13 shows $k_2 = 0$ profiles of the spectra before and after deconvolution. The convective ridge is mildly affected, which is similar to the output of DAMAS2; however, the acoustic region displays strong oscillations. The full spectra map is displayed in Fig. 14, and shows features that are not as

sharp as those from DAMAS2, the overall aspect nonetheless being smooth and sharper than the data before deconvolution.

The main drawback of the method lies in the choice of γ ; since it represents a signal-to-noise ratio and can only be selected from analytical test cases, it is inherently unsuited for the experimental data. Deconvolution of experimental data with the Wiener filter does not seem as robust as using DAMAS2.

VI. Conclusions

Analytical test cases are used to assess the applicability of the Wiener filter and DAMAS2 deconvolution methods to the wave-number-frequency spectra of wall pressure fluctuations beneath a turbulent boundary layer. The array used to sample the data is a rotating antenna developed in previous studies, with 63 aligned microphones and an angular resolution of $\pi/64$.

Deconvolution can be achieved with a Wiener filter, which has the advantage of not being iterative but requires the choice of a regularization parameter. Such a parameter can be chosen from analytical test cases, but its validity is not guaranteed for another set of data, in particular, experimental data. DAMAS2 is seen to satisfactorily converge as long as the relaxation parameter is correctly chosen. While caution should be taken when choosing the number of iterations to apply, the convergence criterion used in this study provides satisfactory results. The antenna's limits to resolving the spectra low frequencies and low acoustic levels, despite deconvolution, have been illustrated.

In light of the present study, a hybrid approach of azimuthal interpolation and deconvolution with DAMAS2 is recommended to better estimate both broadband and narrowband components of the spectra.

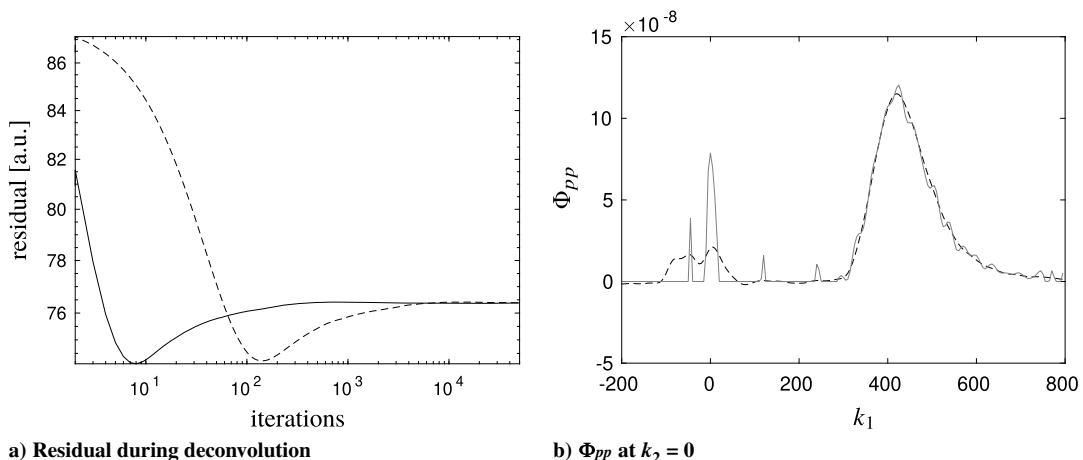


Fig. 11 Deconvolution of experimental data: a) normalized norm of residual — $a = 2.558$ and ---- $a = 43.25$; b) ---- interpolated to $\pi/127$ — deconvolved with $a = 2.558$.

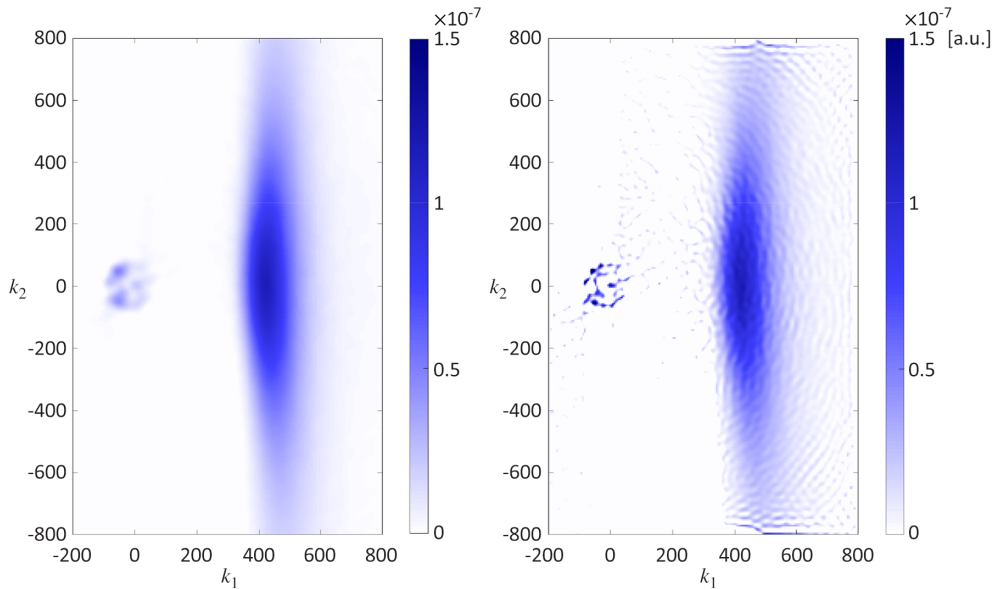


Fig. 12 Φ_{pp} from experimental data interpolated to $\pi/127$, before (left) and after (right) deconvolution with DAMAS2.

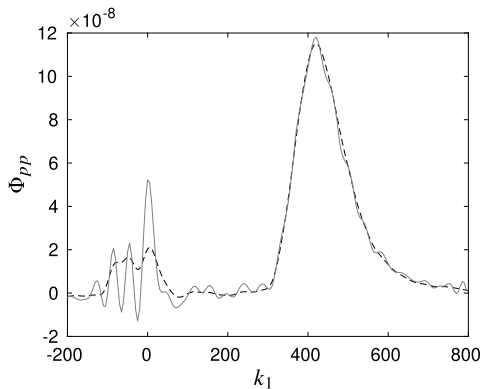


Fig. 13 Φ_{pp} from experimental data interpolated to $\pi/127$ and filtered with a Wiener filter, $\gamma = 0.001$.

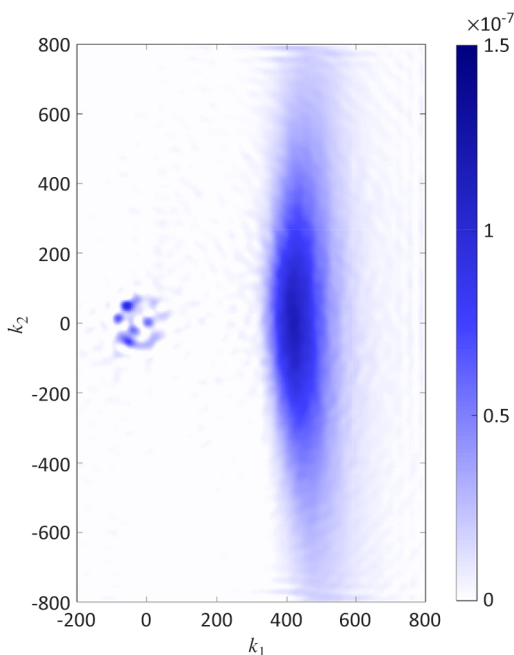


Fig. 14 Φ_{pp} from experimental data interpolated to $\pi/127$ and filtered with a Wiener filter, $\gamma = 0.001$.

Acknowledgement

This project has received funding from the Clean Sky 2 Joint Undertaking under the European Union's Horizon 2020 research and innovation programme under grant agreement No 717084. This work was performed within the framework of the Labex CeLyA of the University of Lyon, within the program "Investissements d'Avenir" (ANR-10-LABX-0060/ANR-16-IDEX-0005) operated by the French National Research Agency. The authors are grateful to Antonio Pereira and Daniel Juvé, who were kind enough to read the manuscript and provide useful comments on matters of signal processing.

References

- [1] Bull, M. K., "Wall-Pressure Fluctuations Beneath Turbulent Boundary Layers: Some Reflections on Forty Years of Research," *Journal of Sound and Vibration*, Vol. 190, No. 3, 1996, pp. 299–315. doi:10.1006/jsvi.1996.0066
- [2] Willmarth, W. W., "Pressure Fluctuations Beneath Turbulent Boundary Layers," *Annual Review of Fluid Mechanics*, Vol. 7, No. 1, 1975, pp. 13–36. doi:10.1146/annurev.fl.07.010175.000305
- [3] Corcos, G. M., "Resolution of Pressure in Turbulence," *Journal of the Acoustical Society of America*, Vol. 35, No. 2, 1963, pp. 192–199. doi:10.1121/1.1918431
- [4] Arguillat, B., Ricot, D., Bailly, C., and Robert, G., "Measured Wavenumber: Frequency Spectrum Associated with Acoustic and Aerodynamic Wall Pressure Fluctuations," *Journal of the Acoustical Society of America*, Vol. 128, No. 4, 2010, pp. 1647–1655. doi:10.1121/1.3478780
- [5] Salze, É., Bailly, C., Marsden, O., Jondeau, E., and Juvé, D., "An Experimental Characterisation of Wall Pressure Wavevector-Frequency Spectra in the Presence of Pressure Gradients," *20th AIAA/CEAS Aeroacoustics Conference*, AIAA Paper 2014-2909, 2909. doi:10.2514/6.2014-2909
- [6] Salze, É., Bailly, C., Marsden, O., Jondeau, E., and Juvé, D., "An Experimental Investigation of Wall Pressure Fluctuations Beneath Pressure Gradients," *21st AIAA/CEAS Aeroacoustics Conference*, AIAA Paper 2015-2909, 2015. doi:10.2514/6.2014-2909
- [7] Ehrenfried, K., and Koop, L., "Comparison of Iterative Deconvolution Algorithms for the Mapping of Acoustic Sources," *AIAA Journal*, Vol. 45, No. 7, 2007, pp. 1584–1595. doi:10.2514/1.26320
- [8] Tiana-Roig, E., and Jacobsen, F., "Deconvolution for the Localization of Sound Sources Using a Circular Microphone Array," *Journal of the Acoustical Society of America*, Vol. 134, No. 3, 2013, pp. 2078–2089. doi:10.1121/1.4816545
- [9] Lylloff, O., Fernández-Grande, E., Agerkvist, F., Hald, J., Tiana Roig, E., and Andersen, M. S., "Improving the Efficiency of Deconvolution Algorithms for Sound Source Localization," *Journal of the Acoustical Society of America*, Vol. 138, No. 1, 2015, pp. 172–180. doi:10.1121/1.4922516

- [10] Dougherty, R., "Extensions of DAMAS and Benefits and Limitations of Deconvolution in Beamforming," *11th AIAA/CEAS Aeroacoustics Conference*, AIAA Paper 2005-2961, 2005.
doi:10.2514/6.2005-2961
- [11] Gabriel, C., Müller, S., Ullrich, F., and Lerch, R., "A New Kind of Sensor Array for Measuring Spatial Coherence of Surface Pressure on a Car's Side Window," *Journal of Sound and Vibration*, Vol. 333, No. 3, 2014, pp. 901–915.
doi:10.1016/j.jsv.2013.09.045
- [12] Cohen, E., and Gloerfelt, X., "Influence of Pressure Gradients on Wall Pressure Beneath a Turbulent Boundary Layer," *Journal of Fluid Mechanics*, Vol. 838, March 2018, pp. 715–758.
doi:10.1017/jfm.2017.898
- [13] Bahr, C. J., and Cattafesta, L. N., "Wavenumber-Frequency Deconvolution of Aeroacoustic Microphone Phased Array Data of Arbitrary Coherence," *Journal of Sound and Vibration*, Vol. 382, No. 10, 2016, pp. 13–42.
doi:10.1016/j.jsv.2016.06.044
- [14] Haxter, S., and Spehr, C., "Infinite Beamforming: Wavenumber Decomposition of Surface Pressure Fluctuations," 2014, pp. 1–10, <http://www.bebec.eu/2014>.
- [15] Ehrenfried, K., and Koop, L., "Pressure Fluctuations Beneath a Compressible Turbulent Boundary Layer," *14th AIAA/CEAS Aero-Acoustics Conference*, AIAA Paper 2008-2800, 2008.
doi:10.2514/6.2008-2800
- [16] Blake, W., *Mechanics of Flow-Induced Sound and Vibration—General Concepts and Elementary Sources*, Vol. 1, Academic Press, Orlando, FL, 1986, pp. 109–111.
- [17] Gonzalez, R. C., and Woods, R. E., *Digital Image Processing*, 2nd ed., Prentice Hall, New Jersey, 2002, pp. 261–264.
doi:10.1007/3-540-27563-0
- [18] Schafer, R. W., Mersereau, R. M., and Richards, M. A., "Constrained Iterative Restoration Algorithms," *Proceedings of the IEEE*, Vol. 69, No. 4, 1981, pp. 432–450.
doi:10.1109/PROC.1981.11987
- [19] Brooks, T. F., and Humphreys, W. M., "A Deconvolution Approach for the Mapping of Acoustic Sources (DAMAS) Determined from Phased Microphone Arrays," *Journal of Sound and Vibration*, Vol. 294, No. 4, 2006, pp. 856–879.
doi:10.1016/j.jsv.2005.12.046
- [20] Brooks, T., and Humphreys, W., "Extension of DAMAS Phased Array Processing for Spatial Coherence Determination (DAMAS-C)," *12th AIAA/CEAS Aeroacoustics Conference (27th AIAA Aeroacoustics Conference)*, AIAA Paper 2006-2654, 2006.
doi:10.2514/6.2006-2654
- [21] Harris, F. J., "On the Use of Windows for Harmonic Analysis with the Discrete Fourier Transform," *Proceedings of the IEEE*, Vol. 66, No. 1, 1978, pp. 51–83.
doi:10.1109/proc.1978.10837
- [22] Coggins, B. E., and Zhou, P., "Polar Fourier Transforms of Radially Sampled NMR Data," *Journal of Magnetic Resonance*, Vol. 182, No. 1, 2006, pp. 84–95.
doi:10.1016/j.jmr.2006.06.016
- [23] Maxit, L., "Simulation of the Pressure Field Beneath a Turbulent Boundary Layer Using Realizations of Uncorrelated Wall Plane Waves," *Journal of the Acoustical Society of America*, Vol. 140, No. 2, 2016, pp. 1268–1285.
doi:10.1121/1.4960516

L. Ukeiley
Associate Editor